# Strain induced photoluminescence from silicon and germanium nanowire arrays

**Guillaume Audoit,[a] Éimhín Ní Mhuircheartaigh,[b] Stephen M. Lipson,[b] Michael A. Morris,[a] Werner J. Blau[b] and Justin D. Holmes*[a]**

*Received 22nd July 2005, Accepted 7th September 2005*
*First published as an Advance Article on the web 29th September 2005*
**DOI: 10.1039/b510532c**



The optical properties of silicon and germanium nanowires grown within the pores of hexagonal mesoporous silica matrices have been characterised by ultraviolet absorption and photoluminescence (PL) spectroscopy. A clear blue-shift in the PL of the semiconductor composite materials was observed as the diameter of the nanowires decreased from 85 to 22 Å. Powder X-ray diffraction revealed that, as the diameter of the confined nanowires decreased, the strain on the crystallographic structure of the nanowires increased, due to escalating lattice expansion, resulting in a shift in the PL maximum to higher energies. The ability to manipulate the optical properties in templated semiconductor nanowires, through strain engineering, has important implications for the design of future optical devices.

## Introduction

The last decade has seen intense interest in nanoscale structures with low dimensionality such as quantum wells (2-D), nanowires (1-D) and quantum dots (0-D).[1] Such materials exhibit remarkable optical and electronic properties and offer a potential means of investigating quantum phenomena as a function of nanostructure size. The 'bottom-up' fabrication of nanodevices, and the ability to manipulate quantum effects, will be critical for technologies that form the basis for the next generation of computing, optical and electronic devices. Already, isolated nanodevices such as light emitting diodes[2] and field effect transistors (FETs)[3] have been synthesized from nanoscale building blocks.

In particular, the discovery of unusual quantum-induced electronic properties, including visible photoluminescence (PL), from nanocrystalline silicon has aroused huge scientific interest.[4] The origin of the PL in silicon is hotly debated, although much of the present controversy arises due to a difficulty in identifying the roles that quantum confinement[5] and surface states[6] have on the band structure in these materials. Lack of control over crystallite size and the inability to create size-monodispersed nanocrystal samples often leads to broadening of PL emission peaks making investigations into the origin of specific PL transitions in nanocrystalline silicon difficult.[7] Additionally, PL originating from Ge nanostructures is less well documented than Si. PL from Ge nanoparticles has been attributed to quantum confinement effects,[8] surface/interface states[9] and defects.[10] Among the number of reports on the synthesis of germanium nanowires,[11–23] nothing has been reported, to our knowledge, on the origin of PL from these 1D structures.

Investigations in our laboratory have focused on preparing ultra high-density arrays of size-monodisperse semiconductor,[24,25] metal and metal oxide nanowires[26] within the pores of mesoporous silica hosts,[27] and anodized aluminium oxide membranes.[28] Encapsulation of nanowires in matrices offers the possibility of both manipulating nanowire arrays into useful configurations whilst also allowing great flexibility to tailor their aspect ratios and optical properties. Methods such as electrochemical deposition and chemical vapour deposition[21] have previously been used to fill porous matrices with precursor material to form nanowires. Our work has focused on using supercritical fluid (SCF) methods to reproducibly form a range of tailor-made high quality silica–nanowire composites. Pore blocking using the SCF protocols is minimized, as the surface tension of a SCF is negligible, resulting in uniform and almost complete filling of the porous structures. Of particular interest to us are the optical and electronic properties of semiconductor nanowire-matrix composite materials. We previously reported that silicon nanowires, with diameters between 4.5 to 7.3 nm, prepared within mesoporous silica powders exhibit high intensity ultraviolet (UV) photoluminescence.[29] We also demonstrated the ability to manipulate the UV-PL of these encased silicon nanowires by controlling the pore size of the silica matrix and hence the diameters of the silicon nanowires grown within them. We argued that the origin of the UV-PL arose due to the intrinsic strain within the nanowire and showed that as the curvature, or strain, of the nanowires increased (with decreasing nanowire diameter), the UV-PL emission maximum was shifted to higher energies. In this manuscript we expand on our previous work and provide a more detailed study on the origin of the optical properties of both silicon and germanium nanowire arrays within mesoporous silica hosts. Nanowires with mean diameters between 22 and 85 Å were investigated and the origin of their optical properties were related to their structural

[a]*Department of Chemistry, Materials Section and Supercritical Fluid Centre, University College Cork, Cork, Ireland. E-mail: j.holmes@ucc.ie; Fax: +353 (0)21 4274097; Tel: +353 (0)21 4903608*
[b]*Materials Ireland Polymer Research Centre, Department of Physics Trinity College Dublin, Dublin 2, Ireland*

characteristics using powder X-ray diffraction (PXRD) and electron microscopy.

## Experimental

### Preparation

The synthesis of tunable hexagonal mesoporous silica (HMS) has been comprehensively described in previous work.[30] Briefly, HMS was prepared by the acid hydrolysis of tetramethoxysilane (TMOS) in the presence of a polyethylene oxide (PEO)–polypropylene oxide (PPO) triblock copolymer surfactant, P85 ($PEO_{26}PPO_{39}PEO_{26}$), P123 ($PEO_{20}PPO_{69}PEO_{20}$) or P65 ($PEO_{20}PPO_{30}PEO_{20}$). The decomposition of TMOS generates methanol which is completely removed using a rotary film evaporator at 40 °C. The resulting gel was then left to condense at 40 °C for one week before calcination at 450 °C. The pore diameter of the HMS prepared was typically between 40 and 70 Å ±10%. Smaller diameter HMS was achieved using the surfactants Brij 35 ($C_{12}EO23$) and Brij 76 ($C_{16}EO_{10}$). Swelling processes using decane[31] were used to obtain HMS with pores sizes above 73 Å *i.e.* 80 Å. Silicon and germanium nanowires were produced within the pores of the HMS using a SCF inclusion-phase technique. In a typical preparation, the HMS was degassed at 200 °C under a flow of Nitrogen for 6 h to remove residual moisture and other pore contaminants. The HMS and the semiconductor precursor (diphenylsilane or diphenylgermane for Si and Ge, respectively) were placed in a high pressure vessel and sealed under a nitrogen atmosphere. The loaded reaction cell was then connected to a high-pressure $CO_2$ pump, *via* a 3-way valve and solvent reservoir, and placed in a tube furnace at 500 °C and 35 MPa for 30 min. Supercritical anhydrous hexane was used as a solvent for silicon nanowire synthesis and supercritical $CO_2$ for germanium inclusion within the HMS. The white HMS loaded into the reaction vessel became reddish after the inclusion of silicon nanowires into the mesopores and dark brown after germanium nanowire inclusion. Two controlled reactions were run in the absence of the semiconductor precursor, HMS (synthesised from P85) was exposed to the same experimental conditions, *i.e.* 500 °C with anydrous hexane pressurized at 35 MPa (SiRef) and 500 °C with $CO_2$ pressurized at 35 MPa (GeRef). In both cases no colour change was noticed and the HMS remain white. The product was then washed in anhydrous hexane, chloroform and ethanol before being dried for analysis. The HMS–nanowire composite materials will be referred as Ge40, Si50 *etc.*, meaning germanium and silicon nanowires encased in a HMS with mean diameters of 40 and 50 Å, respectively. Free standing Ge nanowires were also synthesized from the decomposition of diphenylgermane in supercritical $CO_2$ under the same temperature and pressure conditions as above where the nanowires were grown from some residual silica left in the reaction cell.

### Structural characterization

Powder X-ray diffraction (PXRD) profiles were recorded on a Philips X'Pert diffractometer, equipped with a Cu Kα radiation source and accelerator detector. Height and reflected Stoller slits of 0.2° were used with a programmable divergent slit to maintain a 10 mm footprint at the sample. Sample heights, were determined at $\theta = 2\theta = 0$ at the point when the sample reduced the beam intensity by 50%. Low and high angle scans were performed, respectively giving information about the mesoporous arrangement and the crystallographic structure of the specimens. Surface areas of the calcined HMS were measured on a Micromeritics Gemini 2375 nitrogen adsorption instrument and calculated based upon Brunauer–Emmett–Teller (BET)[32] isotherms. Prior to the adsorption measurements, each sample was degassed for 12 h at 200 °C under a high purity nitrogen flow to remove any residual moisture from within the pores. The mean pore size distribution and pore volume of the calcined silicas was calculated based on the Brunauer–Emmett–Teller (BET) and Barrett–Joyner–Halanda (BJH) models,[33] respectively, from a 40-point BET surface area plot. All of the HMS examined exhibited a characteristic type IV adsorption isotherm profile.[32] In all cases, hysterises was observed in adsorption and desorption isotherms. Adsorption isotherms were used to calculate the pore diameter distributions. A JEOL 2000FX transmission electron microscope (TEM) and a Philips CM200 Super TWIN FEG, both operating at an acceleration voltage of 200 kV, were respectively used for TEM and high-resolution TEM (HRTEM) imaging. Samples were dispersed in ethanol, and a drop of the mixture was placed on a 400 mesh carbon-coated copper grid for investigation.

### Optical characterization

The samples were suspended in anhydrous hexane before collecting UV-visible absorption spectra, the PL spectra were recorded on a Perkin Elmer LS50B spectrofluorimeter. Solid state temperature dependant PL spectra were monitoring using a CCD camera. The samples were placed in a 1 mm quartz cuvette inside a cryostat and photoexcited using the 266 nm beam of a nanosecond Nd:YAG laser. Lifetime measurements were performed at the peak PL wavelength using a 408 nm picosecond laser diode to photoexcite the samples and a photomultiplier tube as the detector.

## Results and discussion

All of the mesoporous silicas prepared in this study showed well-resolved peaks characteristic to well-ordered mesoporous structures. Fig. 1a shows low angle powder X-ray diffraction (PXRD) patterns for calcined mesoporous silica templated from the triblock copolymer surfactants P123, P85 and from the polyoxyethylene ethers Brij 35 and Brij 76. Three well-resolved peaks can be readily indexed to (100), (110) and (200) reflections for a hexagonal mesoporous solid[34] for each of the silicas prepared except for the HMS generated from the Brij 35 surfactant, where only the (100) reflection peak is seen. The absence of second and third order diffraction peaks is commonly observed for mesoporous material templated from short hydrocarbon chain surfactants, such as Brij 35, even if the structure is ordered.[35,36] Transmission electron microscopy (TEM) confirmed that the Brij templated matrixes possessed a highly ordered hexagonal structure (Fig. 1b). Furthermore, Fig. 1a shows the (100) diffraction peak from the swelled P123

 

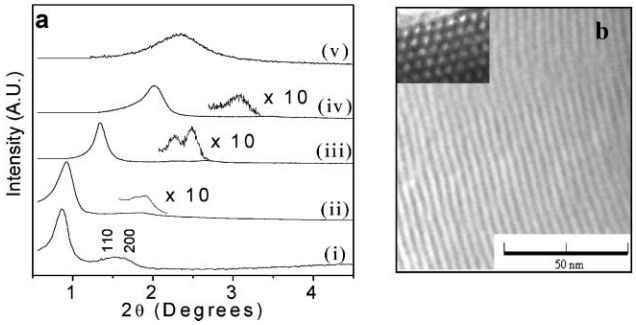


**Fig. 1** (a) Low angle PXRD patterns for HMS templated from surfactants (i) swelled P123, (ii) P123, (iii) P85, (iv) Brij 76 and (v) Brij 35. (b) TEM picture of HMS prepared from Brij 35 before nanowire inclusion. Inset shows an end view of the pores.

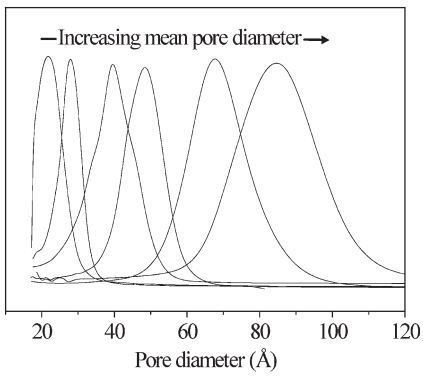


**Fig. 2** Pore size distribution of the HMS with an increasing mean pore size diameter. From left to right: 22, 30, 40, 50, 70 and 85 Å.

templated HMS, which as expected, is shifted towards a lower angle than the regular P123 HMS.

Fig. 2 displays the mean pore size distribution of the HMS before nanowire inclusion. The mean pore diameters of the HMS synthesised in this study, and of the semiconductor nanowires formed within them, range from 22 to 85 Å. Prior to nanowire inclusion, all the HMS displayed type IV adsorption–desorption isotherms characteristic of mesoporous materials.[32] Table 1 lists the physical characteristics of the HMS matrices and the semiconductor–nanocomposite materials as determined by $N_2$ adsorption measurements. All of the HMS exhibit high surface areas ($S_A$) which drastically drops after nanowire inclusion. An almost complete filling of the pores is achieved as partly confirmed by the decrease of the pore volume ($V$). The control samples GeRef and SiRef exhibit the same $S_A$ and $V$ as a P85 silica template (5% difference).

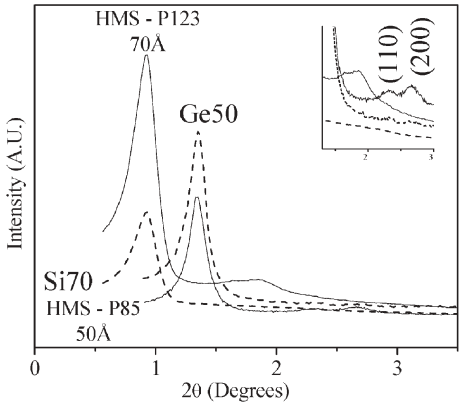


**Fig. 3** Low angle PXRD patterns for the HMS templated from surfactants P123 and P85 after (dashed lines) and before inclusion of Si and Ge respectively. Insets show the (110) and (200) reflection peaks region.

The experimental conditions (high pressure and high temperature) do not drastically affect the structural properties of the mesoporous materials. Fig. 2 also shows that the pore size distribution in the HMS templates increases with increasing pore diameter, as noted by the broadness of the peaks. However the pore size distribution of the HMS remained within a 1 nm range of the mean pore diameter which is considered as an adequate size-dispersity to allow an investigation of size-dependent optical properties.

Fig. 3 shows the low angle PXRD data of two mesoporous silica samples after silicon (Si70) and germanium (Ge50) nanowire inclusion. The position of the intense (100) peak did not change after nanowire inclusion. Clearly, the mesoporous silicas are sufficiently robust to withstand the SCF reaction conditions used in the present experiments. As previously reported the reduced intensity of the (100) peak and the absence of the (110) and (200) peaks noted after Si nanowire inclusion probably arises from the reduced scattering contrast between the matrix scaffold and the nanowires.[37] With the Ge-nanocomposite materials the intensity of the (100) peak is greater compared to the unfilled HMS and the (110) and (200) peaks are still apparent in the PRXD pattern. This observation is a consequence of the greater scattering contrast between Ge and the HMS matrix compared to Si.

Fig. 4 displays TEM images of germanium nanowires, 55 and 65 Å in diameter, encapsulated within an HMS matrix (Ge 55 and Ge65). Ge nanowires can be observed within the channels of the mesopores appearing in black along the pores channels. The BET data confirmed appropriate filling of the

**Table 1** Nitrogen adsorption data for HMS and associated silicon–germanium nanocomposites (surface area ($S_A$) and pore volume ($V$))

| | Mean pore diameter/Å | Pore size distribution/Å | Mean wall thickness/Å | $S_A$/m$^2$ g$^{-1}$ | | | $V$/m$^3$ g$^{-1}$ | | |
|---|---|---|---|---|---|---|---|---|---|
| | | | | HMS | HMS–Si | HMS–Ge | HMS | HMS–Si | HMS–Ge |
| Brij 35 | 22 | 20–26 | 18 | 946 | 54 | 65 | 0.75 | 0.08 | 0.02 |
| Brij 76 | 30 | 28–32 | 20 | 832 | 39 | 54 | 0.69 | 0.05 | 0.04 |
| P 65 | 40 | 35–45 | 20 | 620 | 49 | 55 | 0.83 | 0.03 | 0.02 |
| P 85 | 50 | 45–55 | 25 | 780 | 15 | 32 | 0.95 | 0.01 | 0.04 |
| P123 | 70 | 63–77 | 30 | 520 | 16 | 36 | 0.59 | 0.02 | 0.03 |
| Swelled P123 | 85 | 75–95 | 18 | 500 | 55 | 23 | 0.70 | 0.04 | 0.05 |

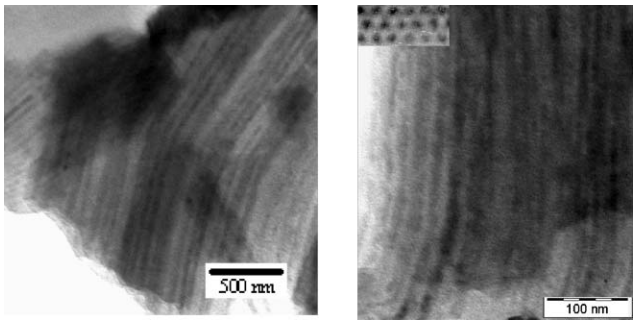


**Fig. 4** TEM pictures of HMS Ge65 and Ge55 after inclusion of germanium nanowires.

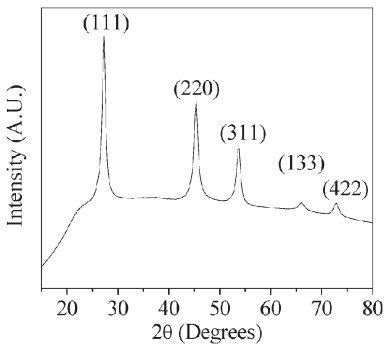


**Fig. 5** High angle PXRD of Ge55 displaying germanium crystalline reflections.

pores of the Ge65 nanocomposite material (Table 1). Fig. 5 shows a high angle PXRD scan obtained from a nanocomposite sample, containing Ge nanowires with a mean diameter of 55 Å (Ge55). The pattern shown is typical of the Ge samples produced in this study. Diffraction peaks arise at 27.5, 45.5, 53.8, 66.3 and 73.1 deg ($2\theta$) and can be indexed to the (111), (220), (311), (331) and (422) reflections of the diamond structure of germanium with a lattice constant $a$ = 5.6794 Å (calculation based on the (111) peak), which corresponds to the literature values for bulk germanium ($a_{bulk}$ = 5.6574 Å).[38]

Bulk silicon is an indirect band-gap semiconductor that traditionally exhibits very weak PL. However, as the size and dimensionality of silicon is decreased, quantum confinement effects become pronounced, resulting in electronic characteristics that are different from the bulk material.[7] In our previous letter we reported an ability to manipulate the UV PL of these encased silicon nanowires by controlling the pore size of the silica matrix and hence the diameter of the silicon nanowires grown within them for Si73, Si50 and Si45 nanocomposite materials.[29] Silicon nanowires prepared within mesoporous matrices exhibit high intensity PL in the UV (2.5–4.5 eV) and the red visible region (1.4–2.1 eV).[29] Subsequent experiments have revealed that the visible PL previously reported was in fact a first harmonic artifact of the UV PL band. UV PL in silicon has previously been ascribed to electron excitation followed by electron-hole pair recombination at oxygen defect centres in silica. However, simple electron-hole recombination in silica could not explain the variation in the UV PL emission wavelength of the

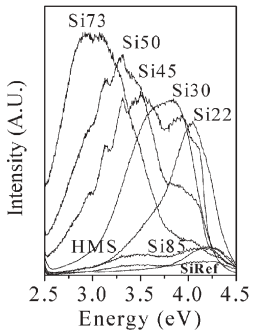


**Fig. 6** UV PL emission spectra for silicon nanowires encased within a mesoporous silica matrix when photo-excited at 4.9 eV.

silica-silicon composite materials as the diameter of the Si nanowire changes. We have argued that this UV PL arose due to the intrinsic strain within the nanowire structures and suggested that as the curvature or strain of nanowires increased, the UV PL emission maximum shifted to higher energies. Fig. 6 shows the UV PL obtained for silicon nanocomposite materials dispersed in anhydrous hexane with mean diameters ranging between 85 and 22 Å. PL emission maximum were observed at 2.93, 3.3, 3.5, 3.75 and 4.02 eV for Si73, Si50, Si45, Si30 and Si22 nanowire–matrix samples respectively. The PL did not result from any organic by-products generated during nanowire formation. For example, the Si reference sample (SiRef) exhibited a similar weak PL as the HMS (Fig. 6). Adequate cleaning and drying of the sample was found to be sufficient to remove any organic contaminants. The decomposition of aromatic organic molecules, such as toluene, in a SCF has previously been used to synthesized carbon nanotubes (CNT) in the presence of a catalyst, such as Fe or FePt.[39] No CNT formation was observed in our samples by TEM. The presence of organic species within the final washed and dried samples was investigated with thermal gravimetric analysis (TGA). No organic species were present. Clearly the PL observed originated from the confined Si nanowires within the HMS matrix.

Fig. 7a shows solid state PL measurements performed on Si73, Si50, Si45 and Si30 after excitation at 266 nm. A blue shift was also noted with decreasing nanowire diameter in the solid state. The same PL measurements have been undertaken on unfilled HMS and the spectra observed were shown to be independent of pore diameter and significantly different than

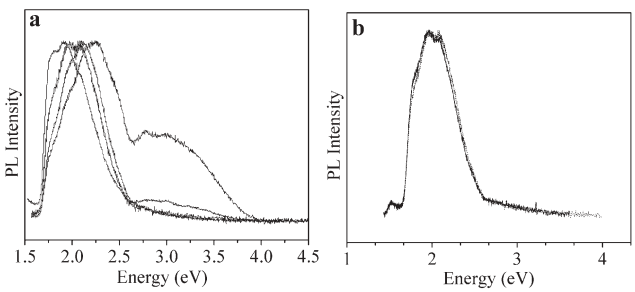


**Fig. 7** Solid state PL spectra at (a) room temperature for (from left to right) Si73, Si50, Si45 and Si30 samples and at (b) 15 K (dotted line) for Si50 compared to room temperature (plain line).

the silicon filled spectra. Low temperature PL measurements in the solid state (15 K) of the Si nanowire samples revealed that the intensity and position of the PL emission maximum remained unchanged from the PL observed at room temperature (Fig. 7b). This result indicates that the observed PL was not phonon assisted, implying that the emission from the Si nanowires is from a direct transition as opposed to the preferred indirect transitions observed in bulk silicon. Further evidence of a direct transition is given by lifetime measurements as shown in Fig. 8 for sample Si45. The biexponential fit gives two decay lifetimes of 1.7 and 5.9 ns with an $R^2$ value of 0.999 associated with a quantum yield 0.13 ($\pm$0.03).[29] In bulk silicon the lifetime of optically created free electrons and holes is up to 4 ms at 23 °C.[40] The lifetime measured here are comparable with the radiative lifetimes observed in direct bandgap semiconductors, *e.g.* $10^9$ s,[40] further suggesting a direct PL transition.

Fig. 9a shows the UV-visible absorbance spectra for Ge nanowires embedded within the pores of HMS. All the materials displayed an absorption edge at approximately 4.2 eV. Quantum confinement effects are expected to affect the band structure of semiconductor nanowires at diameters below their Bohr diameters, *i.e.* 23 nm for Ge and 4.9 nm for Si, shifting their energy levels compared to the bulk. Thus the absorption edge at 4.2 eV for the Ge nanocomposite materials, shown in Fig. 7a, corresponds to one of the two main absorption coefficient peaks of bulk Ge ($E_2$) associated with a direct band-gap transition along the <110> axis of the Ge Brillouin zone.[41] This behaviour differs from the reported absorbance of the Si samples[29] because there is no strong shift with respect to the direct-gap absorption edge of bulk Ge. Fig. 9b shows the PL data for the Ge nanowire arrays with mean diameters of 22, 45, 55 and 65 Å, which reveals an intense emission maximum at 3.58, 3.33, 2.96 and 2.78 eV

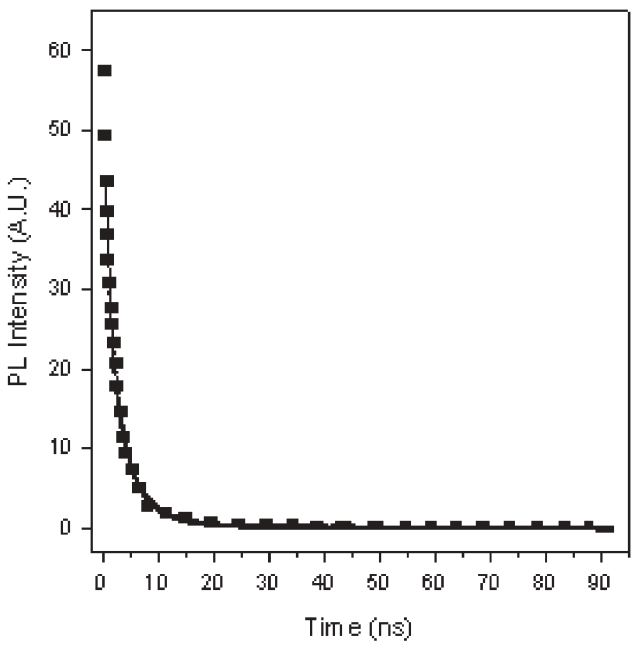


**Fig. 8** PL decay (square) and biexponential fit (solid line) to the PL decay at 590 nm from Si45.

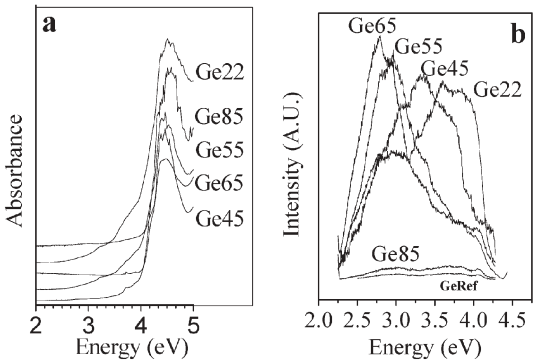


**Fig. 9** (a) Room temperature optical absorbance spectra for germanium nanowires within HMS and dispersed in anhydrous hexane, (b) UV PL emission spectra for Germanium nanowires within tunable mesoporous silica dispersed in anhydrous hexane. Emission after excitation at 4.43 eV.

respectively. The PL from the Ge samples did not result from organic by-products formed during the synthesis of the crystalline Ge nanowires, as confirmed by PL performed on reference samples (GeRef, Fig. 9a) and TGA. A linear blue shift in the PL peak position with decreasing nanowires diameter was observed (Fig. 10). The shape and width of the UV PL peaks also changed as a function of nanowire diameter. The larger diameter nanocomposite materials exhibited broad and overlapping multiple discrete peaks whereas the smaller nanowires materials displayed narrow PL possibly due to the smaller pore size distribution of in templating HMS.

A detailed study of the PXRD peak positions in the Ge and Si nanocomposite materials as a function of pore diameter is shown in Fig. 11 and 12, respectively. The high scattering contrast of Ge and silica enables observation of the diffraction peaks even at small pore diameters where the thickness of the HMS walls is equivalent to the nanowire diameters and hence drastically reduces the scattering contrast. The lattice parameters of the diamond Ge structure calculated form the PXRD peaks position are listed in Table 2 as a function of pore diameter and crystallographic planes. Background determination and subtraction has been carried out using the Sonneveld and Visser model.[42] The estimated interplanar distances are bigger than the corresponding bulk values and moreover they

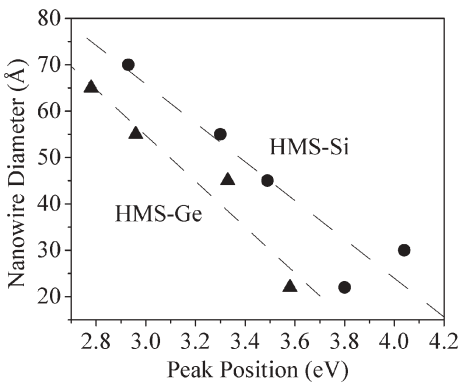


**Fig. 10** UV-PL peak position in function of nanowires diameters for the silicon and germanium composites.

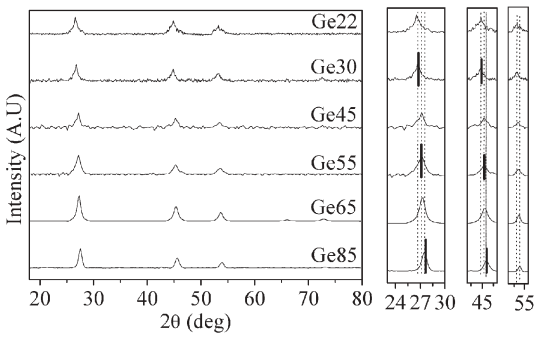


**Fig. 11** High angle PXRD data for the Ge nanocomposites after background subtraction.

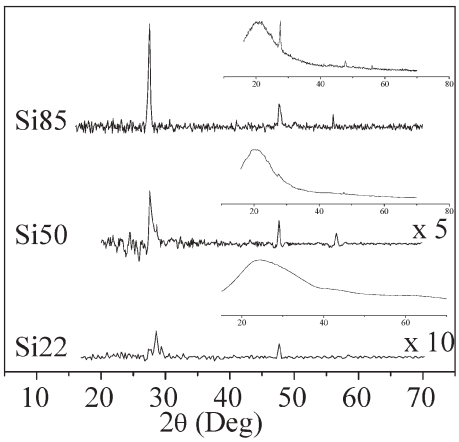


**Fig. 12** High angle PXRD data for the Si nanocomposites showing the (111), (220) and (311) diffraction peaks after background subtraction. Insets show the corresponding raw data.

increase with decreasing nanowires diameter. Fig. 11 reveals an easily observed shift to low $2\theta$ values with decreasing nanowire diameter, corresponding to an increasing lattice expansion. The same trend is observed for the Si nanocomposites materials. Fig. 12 shows the PXRD pattern of the Si samples after background subtraction, due to the similarities of scattering cross-sections of the Si nanowires and the matrix, long scan times (small step size associated with long time per step) are required to see low intensity diffraction features at good signal to noise. The shift in peak position was not as pronounced as the one seen for the Ge samples but however a lattice distortion of 2% plane to plane distance is seen when decreasing down to a 22 Å (Table 3) compare to the bulk Si. This smaller change could possibly be explained by the stronger Si–Si bond compare to Ge–Ge.[43]. A lattice parameter

**Table 3** Plane-to-plane distances ($d$) and corresponding increase factors ($\sigma$) of the HMS–Si

| | P123 85 A | | P85 50 A | | Brij 30 22 A | | Bulk Si |
|---|---|---|---|---|---|---|---|
| Plane | $d$/Å | $\sigma$ (%) | $d$/Å | $\sigma$ (%) | $d$/Å | $\sigma$ (%) | d (A) |
| (111) | 3.136 | — | 3.150 | +0.48 | 3.192 | +1.8 | 3.135 |
| (220) | 2.191 | — | 1.930 | +0.52 | 1.956 | +1.9 | 1.920 |
| (311) | 1.638 | — | 1.637 | — | Not seen | | 1.637 |

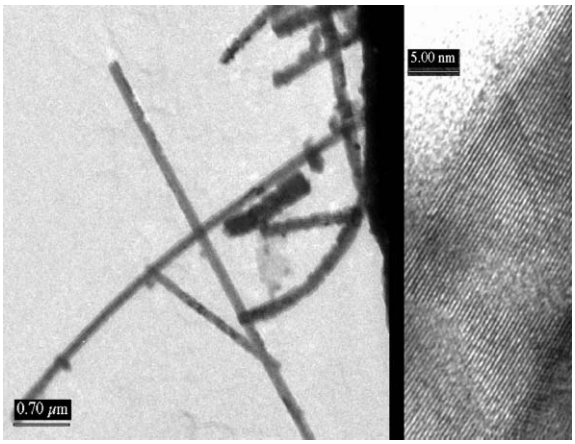


**Fig. 13** High resolution TEM of free-standing Ge nanowires synthesised under the same conditions as the Ge nanocomposites (mean diameters approximately = 140 nm and length of several microns).

change is expected for nanostructured semiconductor material. Lattice contraction has already been reported for Si and SiGe quantum dots, where hydrostatic pressure and surface tension play a dominant role.[44] Here a lattice expansion is more likely to occur as the system is not affected by such forces, since the nanowires are encased within the matrix.[25] Fig. 13 shows a high resolution TEM image of a crystalline free-standing Ge nanowire with a mean diameter of approximately 140 nm. The plane-to-plane distance visible on Fig. 13 is measured at 3.26 Å and is in good agreement with the bulk value for Ge d(111) and very different from the values obtained from the templated nanowires. Hence, the strain imposed by the matrix on the semiconductor nanowires makes these systems very different from their non-templated counterparts, whose internal crystallographic structure corresponds to a local minimum in energy. With the templated materials the matrix is imposing the diameter on the nanowires and so imposing strain into the crystallographic structure resulting in pre-defined nanowire sizes. As the diameter of the nanowires gets smaller, the curvature between the nanowire surface and the pore wall increases leading to further lattice expansion. Strain-induced

**Table 2** Plane-to-plane distances ($d$) and corresponding increase factors ($\sigma$) of the HMS–Ge

| | P123 65 A | | P85 55 A | | P65 45 A | | Brij 76 30 A | | Brij 30 22 A | | Bulk Ge |
|---|---|---|---|---|---|---|---|---|---|---|---|
| Plane | $d$/Å | $\sigma$ (%) | $d$/Å | $\sigma$ (%) | $d$/Å | $\sigma$ (%) | $d$/Å | $\sigma$ (%) | $d$/Å | $\sigma$ (%) | $d$/Å |
| (111) | 3.271 | +0.15 | 3.279 | +0.40 | 3.298 | +0.98 | 3.333 | +2.03 | 3.349 | +2.5 | 3.266 |
| (220) | 2.000 | 0 | 2.003 | +0.13 | 2.001 | +0.05 | 2.024 | +1.18 | 2.022 | +1.1 | 2.000 |
| (311) | 1.707 | +0.08 | 1.712 | +0.37 | 1.717 | +0.68 | 1.724 | +1.04 | 1.719 | +0.77 | 1.706 |
| (422) | 1.297 | +12 | 1.295 | +12 | 1.297 | +12 | 1.303 | +13 | — | — | 1.155 |
| (331) | 1.415 | +9 | 1.296 | −0.16 | — | — | — | — | — | — | 1.298 |

 

PL in the templated nanowires is further substantiated by the fact that only weak PL was observed for Ge85 and Si85, even though the nanowire mean diameter (85 Å) was smaller than the Bohr diameter of Ge. Hence, at large diameters the matrix probably has no effect on the crystallographic lattice. The perceived shift in the PL of these materials, plus the observation of a direct transition in the Si nanowires, suggests that lattice expansion in the nanowires causes a drastic change in the band structure of the materials compared to their bulk counterparts, allowing a high energy radiative pathway to exist.

In conclusion, we have presented evidence to support size-related PL in germanium and silicon nanowires. The absence of any temperature-dependent PL and the relatively fast PL lifetimes indicate that a direct transition is responsible for the UV PL observed from the nanocomposite materials. A crystallographic structure investigation undertaken on the semiconductor nanowires reveals a clear lattice expansion with decreasing diameter possibly introducing discrete energy levels and transitions within the semiconductor band structures. The tunability of the crystallographic deformation and strain, using a mesoporous silica template, allows controllability of the PL which has possible implications for the integration of these materials into future optical and electronic devices.

## Acknowledgements

The authors acknowledge financial support from the Irish Research Council for Science, Engineering and Technology (IRCSET) (Project SC/02/4). The authors would like to thank Stephen Fahy for useful discussions.

## References

1 *Handbook of Nanophase Materials*, ed. A. N. Goldstein, Marcel Dekker, New York, 1997.
2 M. S. Gudiksen, L. J. Lauthon, J. Wang, D. C. Smith and C. M. Lieber, *Nature*, 2002, **415**, 617.
3 Y. Cui and C. M. Lieber, *Science*, 2001, **291**, 851.
4 L. T. Canham, *Appl. Phys. Lett.*, 1990, **57**, 1046.
5 Y. D. Glinka, D. H. Lin, L. P. Hwang, Y. T. Chen and N. H. Tolk, *Phys. Rev. B: Condens. Matter*, 2001, **64**, 8542.
6 G. Ledoux, O. Guillois, D. Porterat, C. Reynaud, F. Huisken, B. Kohn and V. Paillard, *Phys. Rev. B: Condens. Matter*, 2000, **62**, 15942.
7 L. E. Brus, P. F. Szajowski, W. L. Wilson, T. D. Harris, S. Schuppler and P. H. Citrin, *J. Am. Chem. Soc.*, 1995, **117**, 2915.
8 Y. Maeda, N. Tsukamoto and Y. Yazawa, *Appl. Phys. Lett.*, 1991, **59**, 3168.
9 M. Zacharias, J. Christen, J. Blasing and D. Bimberg, *J. Non-Cryst. Solids*, 1996, **198**, 115.
10 M. Zacharias and P. M. Fauchet, *J. Non-Cryst. Solids*, 1998, **227**, 1058.
11 D. Wang and H. Dai, *Angew. Chem., Int. Ed.*, 2002, **41**, 4783.
12 T. Hanrath and B. A. Korgel, *J. Am. Chem. Soc.*, 2002, **124**, 1424.
13 Y. Wu and P. Yang, *Chem. Mater.*, 2000, **12**, 605.
14 Y. Wu and P. Yang, *J. Am. Chem. Soc.*, 2001, **123**, 3165.
15 Z. Zhang, K. Sumitomo, H. Omi and T. Ogino, *Surf. Sci.*, 2002, **497**, 93.
16 X. Lu, K. J. Ziegler, A. Ghezelbash, K. P. Johnston and B. A. Korgel, *Nano Lett.*, 2004, **4**, 969.
17 T. I. Kamins, X. Li and R. Stanley Williams, *Nano Lett.*, 2004, **4**, 503.
18 T. Hanrath and B. A. Korgel, *Adv. Mater.*, 2003, **15**, 437.
19 X. Wu and Y. Tao, *Mater. Res. Bull.*, 2002, **37**, 2179.
20 G. Gu, M. Burghard, G. T. Kim, G. S. Dusberg, P. W. Chiu and V. Krstic, *J. Appl. Phys.*, 2001, **90**, 5747.
21 R. Leon, D. Margolese, G. Stucky and P. M. Petroff, *Phys. Rev. B: Condens. Matter*, 1995, **52**, R2285.
22 Y. F. Zhang, Y. H. Tang, N. Wang, C. S. Lee, I. Bello and S. T. Lee, *Phys. Rev. B: Condens. Matter*, 2000, **61**, 4518.
23 H. Omi and T. Ogino, *Appl. Phys. Lett.*, 1997, **71**, 2163.
24 N. R. B. Coleman, N. O'Sullivan, K. M. Ryan, T. A. Crowley, M. A. Morris, T. R. Spalding, D. C. Steytler and J. D. Holmes, *J. Am. Chem. Soc.*, 2001, **123**, 7010.
25 N. R. B. Coleman, K. M. Ryan, T. R. Spalding, J. D. Holmes and M. A. Morris, *Chem. Phys. Lett.*, 2001, **343**, 1.
26 T. A. Crowley, K. J. Ziegler, D. M. Lyons, D. Erts, H. Olin, M. A. Morris and J. D. Holmes, *Chem. Mater.*, 2003, **15**, 3518.
27 K. M. Ryan, D. Erts, H. Olin, M. A. Morris and J. D. Holmes, *J. Am. Chem. Soc.*, 2003, **125**, 6284.
28 K. J. Ziegler, B. Polyakov, J. S. Kulkarni, T. A. Crowley, K. M. Ryan, M. A. Morris, D. Erts and J. D. Holmes, *J. Mater. Chem.*, 2004, **14**, 585.
29 D. M. Lyons, K. M. Ryan, M. A. Morris and J. D. Holmes, *Nano Lett.*, 2002, **2**, 811.
30 K. M. Ryan, N. R. B. Coleman, D. M. Lyons, J. P. Hanrahan, T. R. Spalding, M. A. Morris, D. C. Steytler, R. K. Heenan and J. D. Holmes, *Langmuir*, 2002, **18**, 4996.
31 J. L. Blin, C. Otjacques, G. Herrier and B. L. Su, *Langmuir*, 2000, **16**, 4229.
32 *Microporosimetry in Comprehensive Supramolecular Chemistry*, ed. H. Lao and C. Detellier, Elsevier Ltd., Oxford, 1996.
33 E. P. Barrett, L. G. Joyner and P. P. Halenda, *J. Am. Chem. Soc.*, 1951, **73**, 373.
34 Q. Huo, D. I. Margolese and G. D. Stucky, *Chem. Mater.*, 1996, **8**, 1147.
35 A. Sayari, M. Kruk and M. Jaroniec, *Catal. Lett.*, 1997, **47**, 147.
36 Y. Liang and R. Anwander, *Microporous Mesoporous Mater.*, 2004, **72**, 153.
37 B. Marler, U. Oberhagemann, S. Vortmann and H. Gies, *Microporous Mater.*, 1996, **6**, 375.
38 *Crystallographic Database for Minerals and Their Structural Analogues*, http://database.iem.ac.ru/mincryst/.
39 D. C. Lee, F. V. Mikulec and B. A. Korgel, *J. Am. Chem. Soc.*, 2004, **126**, 4951–4957.
40 L. E. Brus, *J. Phys. Chem.*, 1994, **98**, 3575.
41 *Physics of Semiconductor Devices, 2nd edn*, ed. S. M. Sze, Wiley, New York, 1981.
42 E. J. Sonneveld and J. W. Visser, *J. Appl. Crystallogr.*, 1975, **8.**
43 *The Strengths of Chemical Bonds*, ed. T. L. Cottrell, London, 1958.
44 M. Dubiel, H. Hofmeister, E. Schurig, E. Wendler and W. Wesch, *Nucl. Instrum. Methods Phys. Res., Sect. B*, 2000, **166**, 871.